Check for updates

Received: 16 July 2020 | Revised: 26 February 2021 | Accepted: 3 March 2021

DOI: 10.1002/glia.23995

GLIA

WILEY

RESEARCH ARTICLE

Super-resolution shadow imaging reveals local remodeling of astrocytic microstructures and brain extracellular space after osmotic challenge

Misa Arizono[1,2] | V.V.G. Krishna Inavalli[1,2] | Stéphane Bancelin[1,2] | Mónica Fernández-Monreal[1,2,3] | U. Valentin Nägerl[1,2]

[1]Interdisciplinary Institute for Neuroscience, Université de Bordeaux, Bordeaux, France

[2]Interdisciplinary Institute for Neuroscience, CNRS UMR 5297, Bordeaux, France

[3]Bordeaux Imaging Center, UMS 3420, CNRS, Université de Bordeaux, US4 INSERM, Bordeaux, France

Correspondence
Misa Arizono and U. Valentin Nägerl, Interdisciplinary Institute for Neuroscience, CNRS UMR 5297, Bordeaux, France.
Email: misa.arizono@u-bordeaux.fr (M. A.) and, valentin.nagerl@u-bordeaux.fr (U. V. N.)

Funding information
Fondation pour la Recherche Médicale, Grant/Award Number: DEQ20160334901; Agence Nationale de la Recherche, Grant/Award Numbers: ANR-17-CE16-0002, ANR-12-BSV4-0014

Abstract

The extracellular space (ECS) plays a central role in brain physiology, shaping the time course and spread of neurochemicals, ions, and nutrients that ensure proper brain homeostasis and neuronal communication. Astrocytes are the most abundant type of glia cell in the brain, whose processes densely infiltrate the brain's parenchyma. As astrocytes are highly sensitive to changes in osmotic pressure, they are capable of exerting a potent physiological influence on the ECS. However, little is known about the spatial distribution and temporal dynamics of the ECS that surrounds astrocytes, owing mostly to a lack of appropriate techniques to visualize the ECS in live brain tissue. Mitigating this technical limitation, we applied the recent SUper-resolution SHadow Imaging technique (SUSHI) to astrocyte-labeled organotypic hippocampal brain slices, which allowed us to concurrently image the complex morphology of astrocytes and the ECS with unprecedented spatial resolution in a live experimental setting. Focusing on ring-like astrocytic microstructures in the spongiform domain, we found them to enclose sizable pools of interstitial fluid and cellular structures like dendritic spines. Upon experimental osmotic challenge, these microstructures remodeled and swelled up at the expense of the pools, effectively increasing the physical interface between astrocytic and cellular structures. Our study reveals novel facets of the dynamic microanatomical relationships between astrocytes, neuropil, and the ECS in living brain tissue, which could be of functional relevance for neuron–glia communication in a variety of (patho)physiological settings, for example, LTP induction, epileptic seizures or acute ischemic stroke, where osmotic disturbances are known to occur.

KEYWORDS
astrocyte, extracellular space, hypo-osmotic stress, STED, super-resolution shadow imaging, synapse

1 | INTRODUCTION

Numerous studies have indicated that astrocytes can powerfully influence neuronal function by modulating the availability of neuroactive substances in the extracellular space (ECS). Astrocytes reportedly do this by rapidly removing potassium and glutamate from the ECS around synapses as well as by releasing gliotransmitters into it (Araque et al., 2014). They may also do so indirectly by modeling the

 © 2021 Wiley Periodicals LLC.

physical shape of the ECS, which could influence the diffusion of these substances and thereby modulate their concentration and time course at the sites of biological action (Syková & Nicholson, 2008).

Indeed, growing evidence suggests that neuron–glia communication and brain homeostasis are regulated by astrocyte-dependent remodeling of the ECS in the healthy and diseased brain.

Whereas a tight association between astrocytic processes and dendritic spines was shown to promote glutamate uptake and gliotransmission (Panatier et al., 2006; Pannasch et al., 2014; Rusakov, 2001), the withdrawal of astrocytic processes from dendritic spines after LTP boosts glutamate spillover at hippocampal synapses (Henneberger et al., 2020). Notably, astrocytes were shown to regulate the flow of interstitial/cerebrospinal fluid via a "glymphatic" system, affecting the clearance of waste products from the brain (Xie et al., 2013). Moreover, astrocytic swelling and ECS shrinkage are a prominent feature of brain pathologies such as edema and epilepsy (Lafrenaye & Simard, 2019), and they exacerbate the disease symptoms by disturbing ion concentration gradients and fluxes and by promoting neuronal hyperexcitability via ephaptic interactions (Andrew, Fagan, Ballyk, & Rosen, 1989; Ballyk, Quackenbush, & Andrew, 1991).

While the ECS is likely to play an important role in these phenomena, it has remained a poorly characterized compartment, whose shape and dynamics around astrocytes and synapses in the neuropil remain largely unknown. Up to now, the ECS has mostly been studied by iontophoretic or fluorescence techniques that quantify the radial spread of diffusible probes released from a point source (Hrabetova, Cognet, Rusakov, & Nägerl, 2018). While these techniques provide precise measurements of bulk biophysical parameters such as volume fraction and tortuosity, they do so over relatively large chunks of brain tissue (>100 μm) and cannot reveal the spatial structure of the ECS. Electron microscopy (EM) offers enough spatial resolution, but it requires tissue fixation, which precludes following live events through time and may introduce artifacts by distorting the tissue and depleting the ECS depending on the fixation protocol.

Indeed, astrocytic process morphology and its relation to synapses are drastically different in the chemically fixed brain compared to the cryo-fixed brain (Korogod, Petersen, & Knott, 2015), calling for the need to develop methods to image these structures in the living state, avoiding any kind of EM processing artifacts.

We addressed this challenge by using the recent SUSHI technique (SUper-resolution SHadow Imaging; [Tønnesen, Inavalli, & Nägerl, 2018]), which can visualize the anatomical organization of the ECS and, by implication, all cellular structures with very high resolution and contrast in living brain tissue. It relies on labeling the interstitial fluid in the ECS with a small but membrane-impermeant fluorescent dye, which casts all cellular structures, including their finest processes, as a sharp shadow under a 3D-STED microscope.

Combining SUSHI with positive fluorescence labeling of astrocytes, we could tease apart the ECS and astrocytes from all other cellular structures, allowing us to examine their dynamic anatomical relationships in living organotypic brain slices.

Focusing on recently described ring-like astrocytic microstructures (Arizono et al., 2020), we observed that they frequently enclosed ECS and synaptic structures like dendritic spines. Upon osmotic challenge, which caused the astrocytes to swell, the aperture of the rings constricted at the expense of the ECS, effectively increasing their interface with the cellular structures inside.

2 | RESULTS

2.1 | Imaging strategy to reveal ECS and astrocyte fine structure

To resolve the fine structure of astrocytes and ECS in organotypic hippocampal brain slices, we employed our recent SUSHI technique based on a custom-built 3D STED microscope (Tønnesen et al., 2018), which provides a volume resolution of under 1 attoliter (∼65 nm in x,y and < 200 nm in z; Figure S1).

The slices were prepared from crossbred transgenic mice (GFAP-Cre/ERT2 and CAG-Floxed ZsGreen) (Hirrlinger, Scheller, Braun, Hirrlinger, & Kirchhoff, 2006), where all astrocytes expressed the fluorescent protein ZsGreen upon hydrotamoxifen treatment (Arizono et al., 2020).

For concurrent visualization of astrocytes and the ECS, we added the fluorescent dye ATTO514 to the ACSF perfusate. We applied linear unmixing to the spectrally detected fluorescence signals, which reduced their crosstalk to under 10% (Tønnesen, Nadrigny, Willig, Wedlich-Söldner, & Nägerl, 2011). To facilitate the perception of contrast and shapes in the images of the densely labeled tissue, we inverted the ATTO514 signal, which more readily reveals the myriad anatomical relationships between ECS, astrocytes, and the other cellular structures (Figure 1a).

We focused our analysis on the *stratum radiatum* of the CA1 area of the hippocampus, where neurites and astroglial processes strongly intermingle, forming "tripartite" synapses (Figure 1b), which have been under intense investigation by neurophysiologists (Durkee & Araque, 2019; Papouin, Dunphy, Tolman, Foley, & Haydon, 2017).

2.2 | Astrocytic microstructures enclose ECS pools and cellular structures

In the dually labeled tissue of astrocytes and ECS (Figure 2a), it was possible to discern cellular structures like dendrites, spines, and astrocytic processes and to distinguish them from the surrounding ECS (Figure 2b).

We focused our attention on the ring-like astrocytic microstructures formed by bulbous "nodes" and tube-like thin "shafts" that we recently identified as ubiquitous anatomical features of protoplasmic astrocytes in the mouse brain (Arizono et al., 2020) (Figure 2). Based on the analysis of z stacks of STED images, most of the ring-like microstructures were actual rings (Figure S2A), while some had a

10981136, 2021, 6, Downloaded from https://onlinelibrary.wiley.com/doi/10.1002/glia.23995 by Portail BibCNRS INP, Wiley Online Library on [11/04/2025]. See the Terms and Conditions (https://onlinelibrary.wiley.com/terms-and-conditions) on Wiley Online Library for rules of use; OA articles are governed by the applicable Creative Commons License

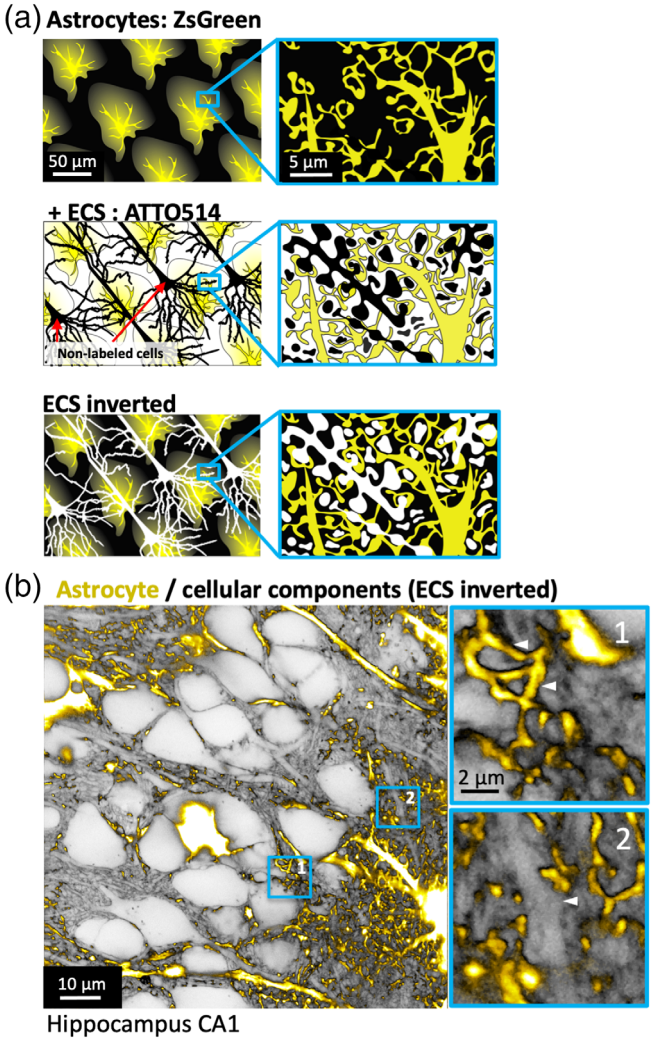


FIGURE 1 Imaging strategy to reveal ECS and astrocyte fine structure. (a) Schematic of astrocyte and ECS imaging using STED microscopy. We used organotypic hippocampal slices where astrocytes are labeled with fluorescent protein ZsGreen (top). By adding fluorescent dye (ATTO514) in the extracellular solution, we can visualize the extracellular space and astrocytes (middle). Inverting the signal reveals the relationship between astrocytes and all the cellular structures in the tissue (bottom). (b) A 3D STED image revealing astrocytic processes infiltrating the neuropil visualized by inverting the ECS image. Zoom-in images show astrocytic processes enwrapping round cellular structures (1, white triangles) and contacting a putative dendrite (2, white triangle) [Color figure can be viewed at wileyonlinelibrary.com]

closed bottom like a cup (Figure S2B). The ring density was 2.7 ± 0.2 rings/100 µm^2 (mean ± *SEM*).

While the rings appeared cytosolically continuous and seamless in the STED images, we cannot rule out the possibility that the rings were partitioned by a very thin membrane-delimited gap, which would be hard to detect by light microscopy, even with STED super-resolution.

To take a closer look, we turned to serial-section EM analysis of chemically fixed organotypic slices. The presence of rings as well as cup cross-sections could both be confirmed by volume reconstructions of the EM data (Figure S3, Video S1).

While we did observe clear cases of astrocytic rings with gaps (Figure S3), consistent with a recent report (Kiyoshi et al., 2020), we also came across rings that appeared seamless, lacking a clear sign of a gap. The definitive answer regarding the existence of seamless rings will probably require more refined EM analysis with cryofixed samples and better image contrast.

We observed that the rings enclosed a variable amount of (non-astrocytic) cellular structures, which oftentimes appeared to be dendritic spines, and ECS filled with interstitial fluid (Figure 2c). Indeed, these cellular structures are comparable to dendritic spine heads in size (Figure S4A), and by dual-labeling of astrocytes and neurons, we confirmed that dendritic spines can be seen inside the rings (Figure S4B). Most of the time (86%) the astrocytic rings enclosed a variable mixture of cellular structures and ECS, but sometimes they appeared to enclose only cellular structures (7%) or only ECS (7%) (Figure 2d).

The median area of the ECS enclosed by the rings was 0.15 µm^2 (Figure 2e), corresponding to 37% of the ring area (Figure 2f), while the median length of the contact zone between ring and ECS was around 1 µm (Figure 2g) corresponding to 38% of the ring perimeter (Figure 2h). The analysis shows that the ECS takes up a sizable portion and not just a thin lining along the inner surface of the astrocytic rings. Moreover, rings were smaller when they only enclosed ECS and most rings contained only a single cellular structure of the simple shape, but larger rings were seen to enclose also multiple or complex-shaped structures (Figure 2i–k).

Given our labeling strategy where the entire accessible ECS and all astrocytes are fluorescently highlighted, we could estimate the volume fractions (VF) of these tissue compartments in the organotypic brain slices. For this, we segmented the two-color images using the recent SpineJ plugin (Levet, Tønnesen, Nägerl, & Sibarita, 2020), which is based on wavelet filtering, and then simply counted the number of pixels that were assigned to the ECS, astrocytes, and all remaining non-labeled structures (Figure S5).

According to this analysis, the ECS accounted for at least 24.4% and the astrocytes for at least 12.6% of the total area of the segmented images. The pixels that were dark, representing all other cellular structures, took up 52.5% (Figure S6). The segmentation algorithm assigned 10.5% of the area to both ECS and astrocytes, because the fluorescence signals overlapped in space, reflecting the limited spatial resolution of our approach (despite the 3D STED) and the residual channel crosstalk (despite spectral unmixing), imposing some irrepressible uncertainty on our VF estimates (Figure S5).

To the extent that the ATTO514 signal (ECS) blurred into the unlabeled structures, their VF (52.5%) represents an underestimate, which is important to keep in mind. By comparison, the ZsGreen signal (astrocytes) should have blurred less into the unlabeled structures, because all astrocytes are surrounded by some lining of ECS and thus do not share a direct border with the other cellular structures, unlike the ECS (Figure S5, S6).

10981136, 2021, 6, Downloaded from https://onlinelibrary.wiley.com/doi/10.1002/glia.23995 by Portail BibCNRS INP, Wiley Online Library on [11/04/2025]. See the Terms and Conditions (https://onlinelibrary.wiley.com/terms-and-conditions) on Wiley Online Library for rules of use; OA articles are governed by the applicable Creative Commons License

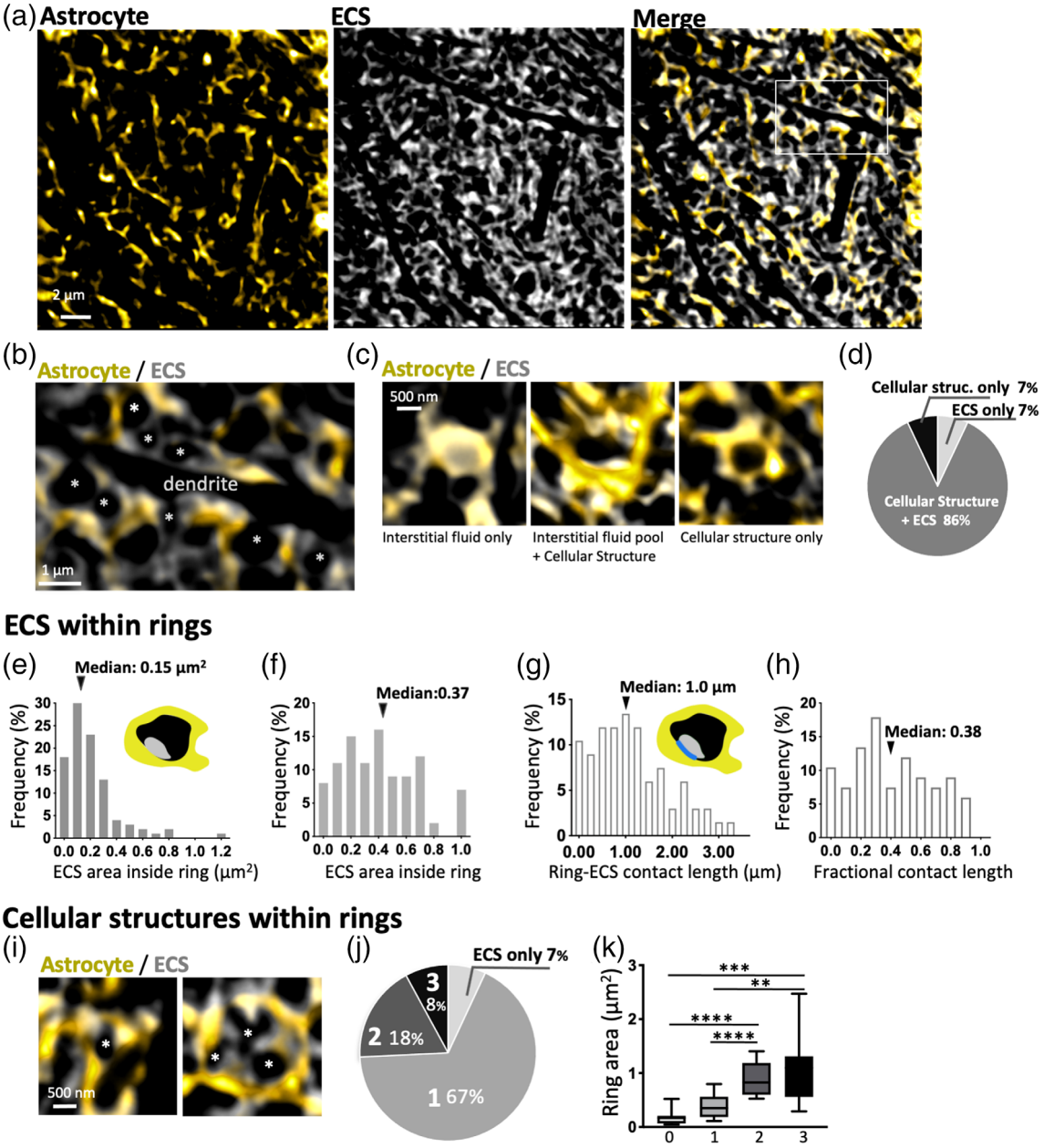


FIGURE 2 Astrocytic microstructures enclose interstitial pools and cellular structures. (a) STED images of reticular structure of astrocytes and ECS visualized by combining positive labeling of astrocytes and staining of ECS. (b) A STED image of astrocyte and ECS showing a negative imprint of a putative dendrite, spines (*) (black), perisynaptic astrocytic processes (yellow) and abundant ECS (gray). (c) Images of rings with only interstitial fluid (left), a pool of interstitial fluid (middle) and without any detectable interstitial fluid (right). (d) Percentage of rings depending on the encircled structure presented in (c). (e) Distribution of ECS area within the rings. (f) Distribution of percentage of ECS area within the rings. (g) Distribution of inner perimeter of the rings in direct contact with the interstitial fluid pool. (h) Distribution of percentage of inner perimeter of the ring in direct contact with the interstitial fluid pool. (i) Example of rings enwrapping cellular structures with simple round geometry (left), and elaborate geometry which may reflect multiple cellular structures (right). (j) Percentage of rings enwrapping 0, 1, 2, and 3 distinguishable negative imprints. (k) Comparison of area inside the ring which are enwrapping 0 (n = 7) 1 (n = 67), 2 (n = 18), and 3 (n = 8) negative imprints. Larger loops enwrap multiple cellular components (five slices; Kruskal-Wallis test, $^{**}p < .01$, $^{***}p < .001$, $^{****}p < .0001$) [Color figure can be viewed at wileyonlinelibrary.com]

2.3 | Astrocytic rings remodel after osmotic challenge, depleting local ECS

Next, we investigated how osmotic challenges might impact this arrangement of astrocytic rings, ECS, and cellular structures, given that astrocytes are known to be highly sensitive to osmotic disturbances induced by neuronal activity or ischemic conditions (Murphy et al., 2017; Yang et al., 2019).

Benefitting from the live-cell imaging approach, we imaged the labeled slices before and during the application of hypo-osmotic stress

10981136, 2021, 6, Downloaded from https://onlinelibrary.wiley.com/doi/10.1002/glia.23995 by Portail BibCNRS INP, Wiley Online Library on [11/04/2025]. See the Terms and Conditions (https://onlinelibrary.wiley.com/terms-and-conditions) on Wiley Online Library for rules of use; OA articles are governed by the applicable Creative Commons License

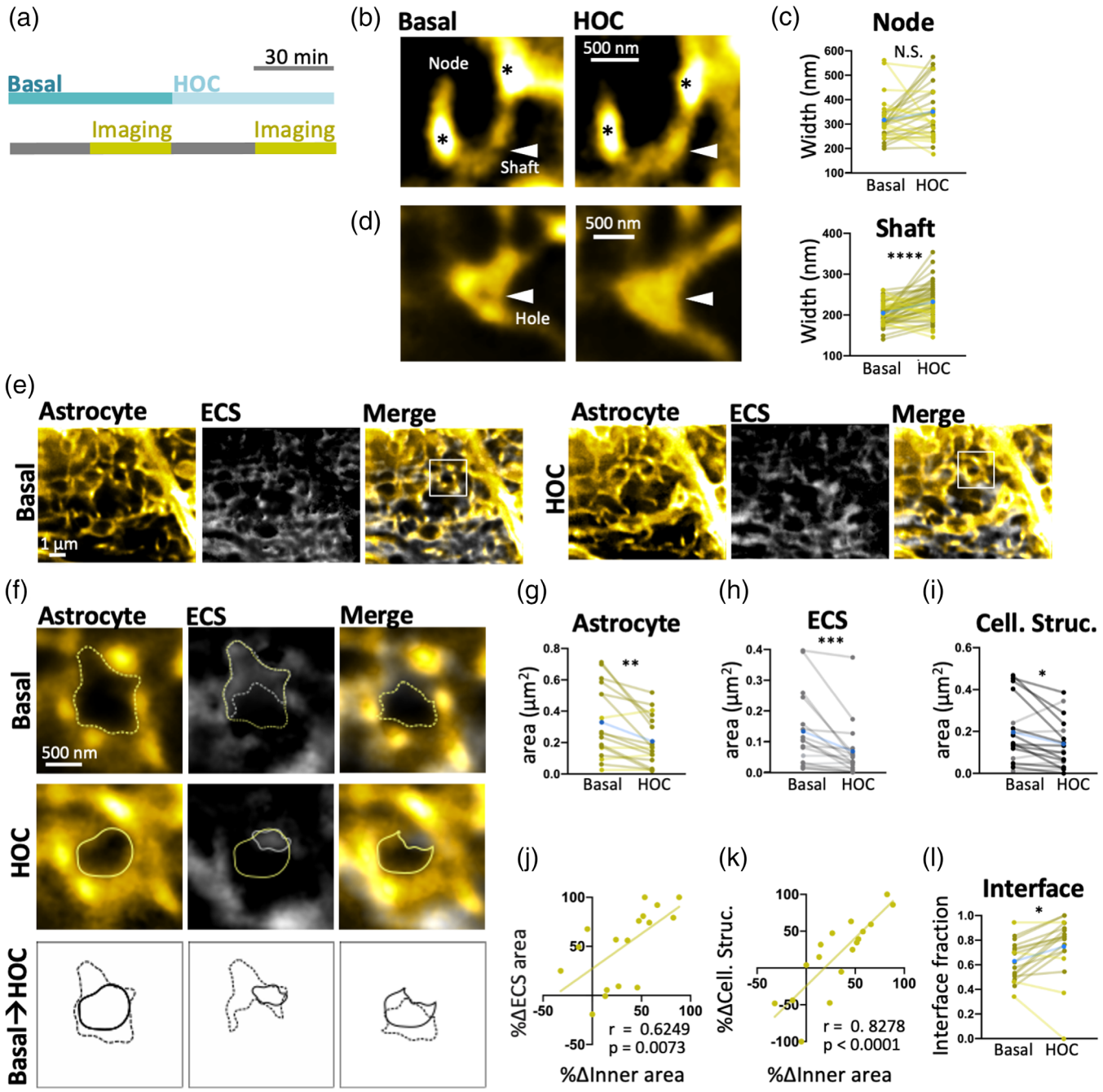


FIGURE 3 Astrocytic microstructures remodel after osmotic challenge, depleting local ECS. (a) Time line of the experiment. (b) STED images of astrocytic processes before (basal) and after hypo-osmotic condition (HOC). Shafts (triangle) connecting nodes (*) selectively swelled. (c) Top: Comparison of astrocytic node width before (basal) and after HOC (n = 30 from four slices; Wilcoxon test, N.S. Not Significant). Bottom: Comparison of astrocytic shaft width before (basal) and after HOC (n = 52 from 4 slices; Wilcoxon test, ****p < .0001). (d) STED images of astrocytic ring before (basal) and after HOC. The hole in the center of the astrocytic ring (white triangle) appears to close in HOC. (e) STED images of reticular structure of an astrocyte and ECS, before (basal, left) and after (HOC, right) HOC. (f) Left: Magnified image of E showing a representative ring (left), encircled ECS (middle), and negative imprint of a cellular structure (right). The bottom panels show the changes before (dotted line) and after (solid line) hypo-osmotic stress. (g–i) Total ring inner area (g), encircled ECS area (h), encircled cellular structure area (i) before (basal) and after HOC (n = 17 from three slices; Wilcoxon test, *p < .05, **p < .01, ***p < .001,). (j) Correlation between fraction change of the ring inner area and fraction change of encircled ECS (n = 17 from three slices; Spearman r = .6249, p = .0073). (k) Correlation between fraction change of the ring inner area and fraction change of encircled cellular structure (n = 17 from three slices; Spearman r = .8278, p < .0001). (l) Fraction of inner perimeter of the loop in contact with cellular structure before and after HOC (n = 17 from three slices; Wilcoxon test, *p < .05). For paired analysis (c, g, h, i, l), blue points indicate the mean values, those that decreased or increased are shown in different shades of color to demonstrate the heterogenous nature of the response [Color figure can be viewed at wileyonlinelibrary.com]

10981136, 2021, 6, Downloaded from https://onlinelibrary.wiley.com/doi/10.1002/glia.23995 by Portail BIoCNRS INP, Wiley Online Library on [11/04/2025]. See the Terms and Conditions (https://onlinelibrary.wiley.com/terms-and-conditions) on Wiley Online Library for rules of use; OA articles are governed by the applicable Creative Commons License

conditions. The hypo-osmotic challenge (HOC) consisted of reducing the osmolarity (i.e., the total number of solute particles per liter of solution) of the normal ACSF, from 300 mOsmol to 200 mOsmol for 30 min (Figure 3a). This is considered a relatively severe form of osmotic stress (Murphy et al., 2017) and a similar reduction (−30% mOsm) was reported to cause sustained astrocytic swelling in vivo (Risher, Andrew, & Kirov, 2009).

The astrocytic microstructures reacted to HOC by remodeling their shape and volume. The morphological changes were heterogeneous in magnitude and direction as well as in the type of structures that were impacted. The astrocytic nodes showed a mixed and modest response, with about 43% of them undergoing shrinkage while 57% showed swelling (Figure 3b,c). By contrast, the astrocytic shafts exhibited a more consistent reaction. Their diameters increased from 204 to 231 nm (median) following the osmotic challenge, which was statistically highly significant (mean ± *SEM*, basal: 204.1 ± 3.9; HOC: 231.5 ± 6.0 nm; $p < .0001$ Wilcoxon test; $N = 51$; Figure 3b,c). Notably, in about 20% of the cases, the ring-like organization of the astrocytic processes disappeared after the osmotic challenge, as if the swelling constricted the area enclosed by the rings (Figure 3d).

A similar tendency was observed after applying a milder form of osmotic stress (250 mOsmol, mHOC) where only shafts swelled (mean ± *SEM*, basal: 213.8 ± 6.2; mHOC: 248.3 ± 7.7; $p < .0001$ Wilcoxon test; $N = 40$; Figure S7A). This effect was absent under control conditions (Figure S7B), indicating that the swelling was not caused by repeated exposures to STED light or the incubation itself.

By co-labeling the ECS, we could also observe how the ECS was affected by the astrocytic remodeling caused by HOC (Figure 3e). We observed that the inner area of the rings decreased (from 0.33 ± 0.056 μm^2 to 0.21 ± 0.039 μm^2 [mean ± *SEM*], Wilcoxon test; $p = .0010$, $N = 17$; Figure 3f,g), consistent with the swelling of the astrocytes, as they delineate the perimeter of this area. At the same time, the areas occupied by the ECS and cellular structures inside the rings decreased substantially (ECS, from 0.13 ± 0.030 μm^2 to 0.066 ± 0.022 μm^2 (mean ± *SEM*), Wilcoxon test; $p = .0001$, $N = 17$; Figure 3f,h; cellular structure, from 0.20 ± 0.038 μm^2 to 0.14 ± 0.029 μm^2 (mean ± *SEM*), Wilcoxon test; $p = .023$, $N = 17$; Figure 3f,i).

The HOC also increased the astrocytic VF by 5%. This increase was mirrored by concomitant reductions in the VF of the ECS and all other cellular structures in some cases, but these reductions were not statistically significant (Figure S8). The lack of statistical significance could reflect the fact that the non-astrocytic VF is much larger, to begin with, making it harder to detect smaller changes.

Nevertheless, the decrease in the inner ring area was highly correlated with a decrease in ECS (Figure 3j) and cellular structures inside the ring (Figure 3k). The zone of contact between the inner side of the astrocytic rings and the cellular structures increased during the osmotic challenge, which might affect the ability of these structures to interact physically or exchange molecular signals at short range (interface fraction, from 0.63 ± 0.040 to 0.75 ± 0.061 (mean ± *SEM*), Wilcoxon test; $p = .011$, $N = 17$; Figure 3l).

3 | DISCUSSION

We used 3D super-resolution microscopy in two colors for volumetric imaging of astrocytes and ECS in living brain slices to reveal their dynamic anatomical relationships induced by an osmotic challenge. The inverse labeling strategy of SUSHI also revealed the surrounding anatomical landscape, making it possible to identify and monitor the neighboring cellular structures alongside the positively labeled astrocytes.

Much of what we know about astrocytic dynamics and swelling (Anderova et al., 2014; Dibaj, Kaiser, Hirrlinger, Kirchhoff, & Neusch, 2007; Risher et al., 2009) has come from studies using light microscopy. However, these studies only reported on the cell bodies and major branches of the astrocytes because of the diffraction limit of light microscopy, which makes it impossible to resolve the spongiform domain, where their highly ramified processes contact synapses in the neuropil.

Quantitative biophysical techniques like TMA^+ iontophoresis have been used to measure changes in the global volume fraction of the ECS as a surrogate for astrocytic swelling (Kume-Kick et al., 2002) (Larsen & MacAulay, 2017), but they can only indicate net changes in overall cellular volume and are insensitive to shape changes.

We focused our attention on ring-like astrocytic microstructures, which are formed by "shafts" and "nodes" of circularly arranged astrocytic processes we described recently (Arizono et al., 2020). The rings typically enclosed cellular structures (such as dendritic spines) and contained sizable pools of interstitial fluid. These pools may correspond in part to the "dead-space microdomains" or "lakes" that were inferred from biophysical studies (Chen & Nicholson, 2000; Tao, Tao, & Nicholson, 2005), or the voluminous patches of ECS that can be seen by EM based on rapid freezing but not chemical fixation (Korogod et al., 2015; Vanharreveld, Crowell, & Malhotra, 1965).

Upon osmotic challenge, the astrocytic shafts grew wider, constricting the aperture of the rings. At the same time, the enclosed ECS and cellular structures shrank or were pushed out of the rings. The astrocytic microstructures tended to take on less complex shapes during osmotic stress, which could be a way to accommodate a larger cell volume without having to add a new cell membrane (Pangršič, Potokar, Haydon, Zorec, & Kreft, 2006).

We obtained clear evidence for astrocytic swelling in response to hypo-osmotic conditions, at the level of global VF and local microstructures. While we did not detect a statistically significant reduction in the global VF of the ECS, we did observe a major compression of ECS structures within astrocytic rings at the local level.

The astrocytic remodeling we documented is likely a direct biophysical consequence of the change in osmotic pressure, which causes a net water movement into the astrocytes, making them swell up at the expense of the ECS (Kume-Kick et al., 2002, Sherpa et al. 2014, reviewed in Stokum, Gerzanich, & Simard, 2016). Interestingly, the nodes remained largely unaffected compared with the shafts. Conceivably, nodes have a sturdier cytoskeletal structure to help them resist osmotic stress and thereby protect the molecular machinery inside of them that can generate Ca^{2+} signals (Arizono et al., 2020).

10981136, 2021, 6, Downloaded from https://onlinelibrary.wiley.com/doi/10.1002/glia.23995 by Portail BibCNRS INP, Wiley Online Library on [11/04/2025]. See the Terms and Conditions (https://onlinelibrary.wiley.com/terms-and-conditions) on Wiley Online Library for rules of use; OA articles are governed by the applicable Creative Commons License

The effects we have observed could have several implications for neuronal function. The local depletion of the ECS may increase the concentration levels of extracellular K^+ and glutamate, and thereby promote neuronal excitability and synaptic transmission (Murphy et al., 2017). The astrocytic swelling and the resultant morphological "de-complexification" may alter the spatial organization of the tripartite synapse and thereby affect the spread of glutamate and its uptake around synapses. Biophysical analysis showed that astrocytic swelling also hinders diffusion in ECS via the formation of dead-space microdomains (Sherpa et al. 2014). The widening of astrocytic shafts may also facilitate the spread of Ca^{2+} signals inside the astrocytes (Arizono et al., 2020), modulating the release of "gliotransmitters" like glutamate. Finally, the swelling of the astrocytic rings may also generate mechanical forces that physically displace adjacent cellular structures and activate mechanosensitive receptors in their membranes (Chighizola et al., 2019).

Our study may be relevant for understanding brain damage such as epilepsy, traumatic brain injury, and stroke (Simard, Kent, Chen, Tarasov, & Gerzanich, 2007), providing a more refined picture of how astrocytic swelling manifests itself within a shifting anatomical landscape of nanoscale dimensions. A variety of molecules such as gap junction proteins (Connexins 30 and 43), Aquaporins, TRP channels, VRAC channels have been implicated in mediating the structural remodeling of astrocytes, however, their exact contributions remain unknown (Lafrenaye & Simard, 2019), which is partly due to the technical difficulties in resolving the underlying anatomical structures.

Applying our novel super-resolution/SUSHI imaging approach to the intact mouse brain in vivo will open up new experimental opportunities to study the complex phenomenology, molecular mechanisms, and functional consequences of astrocytic swelling in a variety of pathophysiologically relevant settings and disease models.

4 | MATERIALS AND METHODS

4.1 | Organotypic hippocampal slice cultures

Organotypic hippocampal slices (Gähwiler, 1981) were dissected from 5 to 7 days old mice, obtained from cross-breeding GFAP-cre (*MGI*:4418665), and Ai6 (JAX: SN007906) mice (Tønnesen et al., 2018), and were cultured 5–8 week in a roller drum at 35°C. ZsGreen expression was induced by 1 μM 4-Hydroxytamoxifen (Sigma-Aldrich) treatment once per week for 5 weeks (Arizono et al., 2020).

Experimental procedures were in accordance with the European Union and CNRS UMR5297 institutional guidelines for the care and use of laboratory animals (Council directive 2010/63/EU).

4.2 | Viral infection of organotypic slices

Microinjectionof Sindbis-Citrine virus into the hippocampal slice for neuronal labeling was performed using a glass pipette connected to Picospritzer (Parker Hannifin). In brief, the virus was injected via a pipette positioned into the CA1 area of the slice by brief pressure pulses (40 ms; 15 psi) 1 day before the experiment (Arizono et al., 2020).

4.3 | ECS labeling and HOC

For ECS staining, ATTO-514 (final concentration ~ 40 μM) was pipetted directly into the chamber while pausing the perfusion. Baseline experiments were performed in artificial cerebrospinal fluid (ACSF) containing 119 mM NaCl, 2.5 mM KCl, 1.3 mM $MgCl_2$, 2.5 mM $CaCl_2$, 26 mM $NaHCO_3$, 1 mM NaH_2PO_4, 20 mM D-glucose, 1 mM Trolox; 300 mOsm; pH 7.3. Hypo-osmotic stress and mild hypo-osmotic stress was applied by perfusing ACSF with reduced NaCl concentration (119 to 69 mM NaCl for 200 mOsm, 119 to 94 mM NaCl for 250 mOsm stress, respectively). Perfusion rate was 2 ml/min and the temperature was 32°C. For ECS staining, ATTO-514 (final concentration ~ 40 μM) was pipetted directly into the chamber while pausing the perfusion.

4.4 | 3D STED microscopy

We used a home-built 3D STED microscope constructed around an inverted microscope body (Leica DMI6000 CS) with a 1.3 NA glycerol immersion objective (HC PL APO 63X, Leica Microsystems, Germany) equipped with a correction collar to compensate spherical aberrations and thus to allow imaging deeper inside tissue as described previously (Urban, Willig, Hell, & Nägerl, 2011). The microscope uses pulsed excitation at 488 nm (PDL 800-D, PicoQuant) and pulsed quenching at 594 nm. The quenching wavelength is obtained from an optical parametric oscillator pumped at 732 nm by a Ti:sapphire femtosecond laser (MaiTai, SpectraPhysics). The 3D resolution enhancement was achieved by splitting the STED beam into two beams; imposing one to a 2π delay vortex phase mask for lateral resolution and the other to an annular π delay phase mask for axial resolution, and subsequently recombining them, as described previously (Tønnesen et al., 2018). The combination of ZsGreen and ATTO 514 signals were spectrally separated using a 514 nm long-pass dichroic mirror and detected with two avalanche photodiodes (Tønnesen et al., 2011).

4.5 | STED image acquisition parameters

STED z-stack images were typically acquired with the imaging conditions (1) $20 \times 20 \times 2$ μm^3, pixel size 19.53 nm, z plane 80 nm $\times$ 25 planes for single z-stacks, and (2) $10 \times 10 \times 0.5$ μm^3, pixel size 19.53 nm, z plane 80 nm $\times$ 5 planes for paired image acquisitions in basal and hypo-osmotic conditions. Image acquisition was controlled by the Imspector software.

4.6 | Image processing and analysis

All STED images were deconvolved using the Huygens Professional (SVI) software. ZsGreen (astrocyte) and ATTO 514 (ECS) or Citrine (neuronal labeling) were spectrally unmixed using a plugin for ImageJ ("Spectral Unmixing" by J. Walter). In brief, we selected regions of interest in the raw images of the two channels that contained either

10981136, 2021, 6, Downloaded from https://onlinelibrary.wiley.com/doi/10.1002/glia.23995 by Portail BIBCNRS INP, Wiley Online Library on [11/04/2025]. See the Terms and Conditions (https://onlinelibrary.wiley.com/terms-and-conditions) on Wiley Online Library for rules of use; OA articles are governed by the applicable Creative Commons License

only background, ZsGreen or ATTO 514 signal. The plugin then computed the unmixing coefficients, which were used to unmix the fluorescence signals in the acquired images (Tønnesen et al., 2011).

To measure astrocytic process width, we used the ImageJ plugin-SpineJ (Levet et al., 2020). Nodes were defined as bright bulbous structures and shafts as tube-like thin structures. For volume fraction, we also used wavelet-based binarization function of SpineJ which faithfully delineated the fluorescent signal (Figure S5). For parameters regarding the rings, the analysis was performed by manual tracing of the structures and subsequently calculating the area or perimeter using ImageJ software (NIH). z-stack images were used to confirm that they are ring-like in 3D and not a cup with a bottom (Figure S2).

4.7 | Sample preparation for EM

Five weeks-in-culture organotypic slices were fixed with 2% paraformaldehyde, 2% glutaraldehyde, and 2 mM of $CaCl_2$ in 0.15 M sodium cacodylate buffer, overnight at 4°C. After three washes in cacodylate buffer with 2 mM $CaCl_2$, we followed the procedure for heavy-metal staining (NCMIR protocol) to enhance membrane contrast in tissue (https://ncmir.ucsd.edu/sbem-protocol). Briefly, tissue was post-fixed with a mixture of 2% osmium tetroxide and 1.5% potassium ferrocyanide 1 hr on ice, followed by incubation with a 1% thiocarbohydrazide in ddH_2O for 20 min at room temperature. Samples were then incubated with 2% OsO_4 in ddH_2O for 30 min at room temperature, followed by 1% aqueous uranyl acetate overnight at 4°C. Finally, slices were subjected to a Walton's lead aspartate staining at 60°C for 30 min. After dehydrations in the graded concentration of ice-cold ethanol (20–50–70–90%), samples were incubated twice with 100% anhydrous ice-cold acetone. Samples were flat-embedded in epon resin. After polymerization, blocks were fixed in a pin for the 3View system (Gatan Inc.) holder. To remove ionic charges or SEM acquisition, samples were covered with silver resin and trimmed for the ultramicrotome of the 3View installed in a Gemini3-SEM.

4.8 | Serial block face scanning electron microscopy

Samples were imaged in a Zeiss Gemini3-SEM operating at a voltage of 1.5 kV with a 20 μm condenser aperture. The SEM was operated in high vacuum. The images were acquired at high-magnification mode with a pixel size of 10 nm and a pixel time of 1 μs in the x/y plane, and 30 nm along the z-axis. A total of 1,000 images were acquired in two different regions (~30 μm). The microscope is equipped with a "Focal Charge Compensation" system operating at 60% to increase SEM resolution.

4.9 | Image analysis of EM images

Astrocytic cytosol was identified initially by the cell body, which has an irregular shape containing glycogen granules and from there by the processes, which exhibit complex shapes infiltrating the neuropil. EM images are segmented using "Carving" function of iLastik software, which is based on a seeded watershed algorithm (https://www.ilastik.org/documentation/carving/carving). The beginning and end of rings were defined by where the rings opened up (Video S1). 3D images were generated using "3D viewer" function of ImageJ.

ACKNOWLEDGMENTS

The study was supported by research grants from the Agence Nationale de la Recherche (ANR-12-BSV4-0014 and ANR-17-CE16-0002) and Fondation pour la Recherche Médicale (DEQ20160334901). M. A. was supported by a postdoctoral fellowship from JSPS (Japan). The electron microscopy was done in the Bordeaux Imaging Center, a service unit of the CNRS-INSERM and Bordeaux University, member of the national infrastructure France BioImaging supported by the French National Research Agency (ANR-10-INBS-04). We thank J. Angibaud for preparing organotypic slices. We thank J. Badaut and members of the Nägerl team for comments on the manuscript.

COMPETING INTERESTS

The authors declare no competing interests.

DATA AVAILABILITY STATEMENT

The data that support the findings of this study are available from the corresponding author upon reasonable request. Further information and requests for resources and reagents should be directed to and will be provided by the lead contact, U.Valentin Nägerl (valentin.nagerl@u-bordeaux.fr).

ORCID

Misa Arizono https://orcid.org/0000-0002-7726-6531
V.V.G. Krishna Inavalli https://orcid.org/0000-0002-7100-0214
Stéphane Bancelin https://orcid.org/0000-0001-6328-0423
Mónica Fernández-Monreal https://orcid.org/0000-0001-7278-448X
U. Valentin Nägerl https://orcid.org/0000-0001-6831-9008

REFERENCES

Anderova, M., Benesova, J., Mikesova, M., Dzamba, D., Honsa, P., Kriska, J., … Vargova, L. (2014). Altered astrocytic swelling in the cortex of α-syntrophin-negative gfap/egfp mice. *PLoS One*, *9*(11), e113444.

Andrew, R. D., Fagan, M., Ballyk, B. A., & Rosen, A. S. (1989). Seizure susceptibility and the osmotic state. *Brain Research*, *498*(1), 175–180.

Araque, A., Carmignoto, G., Haydon, P. G., Oliet, S. H., Robitaille, R., & Volterra, A. (2014). Gliotransmitters travel in time and space. *Neuron*, *81*(4), 728–739.

Arizono, M., Inavalli, V. V. G. K., Panatier, A., Pfeiffer, T., Angibaud, J., Levet, F., … Nägerl, U. V. (2020). Structural basis of astrocytic ca2+ signals at tripartite synapses. *Nature Communications*, *11*(1), 1906.

Ballyk, B. A., Quackenbush, S. J., & Andrew, R. D. (1991). Osmotic effects on the ca1 neuronal population in hippocampal slices with special reference to glucose. *Journal of Neurophysiology*, *65*(5), 1055–1066.

Chen, K. C., & Nicholson, C. (2000). Changes in brain cell shape create residual extracellular space volume and explain tortuosity behavior during osmotic challenge. *Proceedings of the National Academy of Sciences of the United States of America*, *97*(15), 8306–8311.

10981136, 2021, 6, Downloaded from https://onlinelibrary.wiley.com/doi/10.1002/glia.23995 by Portail BibCNRS INP, Wiley Online Library on [11/04/2025]. See the Terms and Conditions (https://onlinelibrary.wiley.com/terms-and-conditions) on Wiley Online Library for rules of use; OA articles are governed by the applicable Creative Commons License

Chighizola, M., Dini, T., Lenardi, C., Milani, P., Podestà, A., & Schulte, C. (2019). Mechanotransduction in neuronal cell development and functioning. *Biophysical Reviews*, *11*(5), 701–720.

Dibaj, P., Kaiser, M., Hirrlinger, J., Kirchhoff, F., & Neusch, C. (2007). Kir4.1 channels regulate swelling of astroglial processes in experimental spinal cord edema. *Journal of Neurochemistry*, *103*(6), 2620–2628.

Durkee, C. A., & Araque, A. (2019). Diversity and specificity of astrocyte-neuron communication. *Neuroscience*, *396*, 73–78.

Gähwiler, B. H. (1981). Organotypic monolayer cultures of nervous tissue. *Journal of Neuroscience Methods*, *4*(4), 329–342.

Henneberger, C., Bard, L., Panatier, A., Reynolds, J. P., Kopach, O., Medvedev, N. I., … Rusakov, D. A. (2020). Ltp induction boosts glutamate spillover by driving withdrawal of perisynaptic astroglia. *Neuron*, *108*(5), 919–936.e11.

Hirrlinger, P. G., Scheller, A., Braun, C., Hirrlinger, J., & Kirchhoff, F. (2006). Temporal control of gene recombination in astrocytes by transgenic expression of the tamoxifen-inducible dna recombinase variant creert2. *Glia*, *54*(1), 11–20.

Hrabetova, S., Cognet, L., Rusakov, D. A., & Nägerl, U. V. (2018). Unveiling the extracellular space of the brain: From super-resolved microstructure to in vivo function. *The Journal of Neuroscience*, *38*(44), 9355–9363.

Kiyoshi, C. M., Aten, S., Arzola, E. P., Patterson, J. A., Taylor, A. T., Du, Y., Guiher, A. M., Philip, M., Camacho, E. G., Mediratta, D., Collins, K., Benson, E., Kidd, G., Terman, D., Zhou, M. 2020. Ultrastructural view of astrocyte-astrocyte and astrocyte-synapse contacts within the hippocampus. *bioRxiv*. 358200. https://doi.org/10.1101/2020.10.28.358200

Korogod, N., Petersen, C. C., & Knott, G. W. (2015). Ultrastructural analysis of adult mouse neocortex comparing aldehyde perfusion with cryo fixation. *eLife*, *4*, e05793.

Kume-Kick, J., Mazel, T., Vorisek, I., Hrabětová, S., Tao, L., & Nicholson, C. (2002). Independence of extracellular tortuosity and volume fraction during osmotic challenge in rat neocortex. *The Journal of Physiology*, *542*(Pt 2), 515–527.

Lafrenaye, A. D., & Simard, J. M. (2019). Bursting at the seams: Molecular mechanisms mediating astrocyte swelling. *International Journal of Molecular Sciences*, *20*(2), 330. https://doi.org/10.3390/ijms20020330.

Larsen, B. R., & MacAulay, N. (2017). Activity-dependent astrocyte swelling is mediated by ph-regulating mechanisms. *Glia*, *65*(10), 1668–1681.

Levet, F, Tønnesen, J, Nägerl, UV, Sibarita, JB. 2020. Spinej: A software tool for quantitative analysis of nanoscale spine morphology. Methods.

Murphy, T. R., Davila, D., Cuvelier, N., Young, L. R., Lauderdale, K., Binder, D. K., & Fiacco, T. A. (2017). Hippocampal and cortical pyramidal neurons swell in parallel with astrocytes during acute hypoosmolar stress. *Frontiers in Cellular Neuroscience*, *11*, 275.

Panatier, A., Theodosis, D. T., Mothet, J. P., Touquet, B., Pollegioni, L., Poulain, D. A., & Oliet, S. H. (2006). Glia-derived d-serine controls nmda receptor activity and synaptic memory. *Cell*, *125*(4), 775–784.

Pangršič, T., Potokar, M., Haydon, P. G., Zorec, R., & Kreft, M. (2006). Astrocyte swelling leads to membrane unfolding, not membrane insertion. *Journal of Neurochemistry*, *99*(2), 514–523.

Pannasch, U., Freche, D., Dallérac, G., Ghézali, G., Escartin, C., Ezan, P., … Rouach, N. (2014). Connexin 30 sets synaptic strength by controlling astroglial synapse invasion. *Nature Neuroscience*, *17*(4), 549–558.

Papouin, T., Dunphy, J., Tolman, M., Foley, J. C., & Haydon, P. G. (2017). Astrocytic control of synaptic function. *Philosophical Transactions of the Royal Society of London. Series B, Biological Sciences*, *372*(1715).

Risher, W. C., Andrew, R. D., & Kirov, S. A. (2009). Real-time passive volume responses of astrocytes to acute osmotic and ischemic stress in cortical slices and in vivo revealed by two-photon microscopy. *Glia*, *57*(2), 207–221.

Rusakov, D. A. (2001). The role of perisynaptic glial sheaths in glutamate spillover and extracellular ca(2+) depletion. *Biophysical Journal*, *81*(4), 1947–1959.

Sherpa, A. D., van de Nes, P., Xiao, F., Weedon, J., & Hrabetova, S. (2014). Gliotoxin-induced swelling of astrocytes hinders diffusion in brain extracellular space via formation of dead-space microdomains. *Glia*, *62*(7), 1053–1065. https://doi.org/10.1002/glia.22661.

Simard, J. M., Kent, T. A., Chen, M., Tarasov, K. V., & Gerzanich, V. (2007). Brain oedema in focal ischaemia: Molecular pathophysiology and theoretical implications. *The Lancet Neurology*, *6*(3), 258–268.

Stokum, J. A., Gerzanich, V., & Simard, J. M. (2016). Molecular pathophysiology of cerebral edema. *Journal of Cerebral Blood Flow and Metabolism*, *36*(3), 513–538.

Syková, E., & Nicholson, C. (2008). Diffusion in brain extracellular space. *Physiological Reviews*, *88*(4), 1277–1340.

Tao, A., Tao, L., & Nicholson, C. (2005). Cell cavities increase tortuosity in brain extracellular space. *Journal of Theoretical Biology*, *234*(4), 525–536.

Tønnesen, J., Inavalli, V. V. G. K., & Nägerl, U. V. (2018). Super-resolution imaging of the extracellular space in living brain tissue. *Cell*, *172*(5), 1108–1121 e1115.

Tønnesen, J., Nadrigny, F., Willig, K. I., Wedlich-Söldner, R., & Nägerl, U. V. (2011). Two-color sted microscopy of living synapses using a single laser-beam pair. *Biophysical Journal*, *101*(10), 2545–2552.

Urban, N. T., Willig, K. I., Hell, S. W., & Nägerl, U. V. (2011). Sted nanoscopy of actin dynamics in synapses deep inside living brain slices. *Biophysical Journal*, *101*(5), 1277–1284.

Vanharreveld, A., Crowell, J., & Malhotra, S. K. (1965). A study of extracellular space in central nervous tissue by freeze-substitution. *The Journal of Cell Biology*, *25*, 117–137.

Xie, L., Kang, H., Xu, Q., Chen, M. J., Liao, Y., Thiyagarajan, M., … Nedergaard, M. (2013). Sleep drives metabolite clearance from the adult brain. *Science*, *342*(6156), 373–377.

Yang, J., Vitery, M. D. C., Chen, J., Osei-Owusu, J., Chu, J., & Qiu, Z. (2019). Glutamate-releasing swell1 channel in astrocytes modulates synaptic transmission and promotes brain damage in stroke. *Neuron*, *102*(4), 813–827 e816.

SUPPORTING INFORMATION

Additional supporting information may be found online in the Supporting Information section at the end of this article.

How to cite this article: Arizono M, Inavalli VK, Bancelin S, Fernández-Monreal M, Nägerl UV. Super-resolution shadow imaging reveals local remodeling of astrocytic microstructures and brain extracellular space after osmotic challenge. *Glia*. 2021;69:1605–1613. https://doi.org/10.1002/glia.23995

10981136, 2021, 6, Downloaded from https://onlinelibrary.wiley.com/doi/10.1002/glia.23995 by Portail BibCNRS INP, Wiley Online Library on [11/04/2025]. See the Terms and Conditions (https://onlinelibrary.wiley.com/terms-and-conditions) on Wiley Online Library for rules of use; OA articles are governed by the applicable Creative Commons License